Supplementary Information

Modulate energy barriers and reaction pathways via dual-ligands engineering for enabling efficient NO removal and hydrogen production

Kaili Wu [a,1], Bin Yao [a,*1], Yan Lin [a], Yirui Qiu [a], Lang Sun [a], Youzhou He [a], Yongcheng Feng [a], Min Fu [a], Chenghua Zhang [b,*], Xingyan Liu [a], Siping Wei [c,*]

[a] Chongqing Key Laboratory of Environmental Catalysis, College of Environment and Resources, Chongqing Technology and Business University, Chongqing 400067, China.
[b] School of Pharmacy, North Sichuan Medical College, Nanchong 637100, China.
[c] Central Nervous System Drug Key Laboratory of Sichuan Province, Department of Medicinal Chemistry, School of Pharmacy, Southwest Medical University, Luzhou 646000, China.

[1] These authors contributed equally to this work and should be considered co-first authors.

[*] Corresponding authors. E-mail addresses: yaobin@ctbu.edu.cn (B. Yao), zchua@nsmc.edu.cn (C. Zhang), wei1225@swmu.edu.cn (S. Wei).

Table of content

Supplementary Texts....4

Text S1. Materials....4

Text S2. The synthesis of NM125-D-A^0....4

Text S3. Characterization of photocatalysts....4

Text S4. Photocatalytic water decomposition to produce hydrogen....5

Text S5. Photocatalytic NO purification....6

Text S6. *In-situ* DRIFTS spectra....7

Text S7. Electrochemical measurements....7

Text S8. Theoretical calculations....8

Supplementary Figures....9

Fig. S1 Pore Parameters for NM125, NM125-D and NM125-D-A....9

Fig. S2 (a) O 1s of NM125, NM125-D and NM125-D-A and (b) Au 4f of NM125-D-A....9

Fig. S3 TEM of (a-b) NM125-D and (c-d) NM125-D-A.....9

Fig. S4 TEM-EDS elemental mapping of NM125-D-A....10

Fig. S5 XRD pattern of NM125-D-A before and after NO removal....10

Fig. S6 (a) XRD pattern and (b) photocatalytic hydrogen evolution of NM125-D-A^0 and NM125-D-A 10

Fig. S7 *In-situ* infrared spectra of NO adsorption processes over (a) NM125 and (b) NM125-D-A 11

Fig. S8 Density of States (DOS) of NM125, NM125-D and NM125-D-A....11

Fig. S9 Adsorption of O_2 and H_2O molecule on different Ti sites in NM125-D-A.....12

Fig. S10 Possible photocatalytic mechanism of NM125....12

Supplementary Tables....14

Table. S1. Au contents (wt %) of different samples characterized by ICP-OES....14

Table. S2. Specific Surface Area and Pore Parameters for NM125, NM125-D and NM125-D-A 14

Table. S3. Comparison of photocatalytic hydrogen evolution data of MOF-based photocatalysts reported in recent years....14

Table. S4. Comparison of photocatalytic NO removal data of MOF-based photocatalysts reported

in recent years 16
Table. S5. Band structure of NM125, NM125-D and NM125-D-A 17
Table. S6. Substances corresponding to infrared peak values during dark adsorption and photocatalytic oxidation stages 17
Table. S7. The reaction pathway for NO removal 18
Table. S8. The reaction pathway for H_2 production 19
References 19

Supplementary Texts

Text S1. Materials

During the experiment, 2-amino-terephthalic acid (NH_2-BDC, 98%, Aladdin), 2,2'-bipyridine-5,5'-dicarboxylic acid (DPDC, 98%, Zhengzhou Alfa Chemical Co., Ltd), Titanium tetraisopropanolate (TTIP, 99%, Adamas), N, N-dimethylformamide (DMF, 99%, Adamas), Methyl alcohol (MeOH, 99%, Adamas), and Tetrachloroauric acid trihydrate ($HAuCl_4 \cdot 3H_2O$, 99%, Adamas) were used. All reagents are analytical grade, which can be used directly without treatment.

Text S2. The synthesis of NM125-D-A^0

NM125-D-A (80 mg) was added to deionized water (10 mL), followed by the addition of glucose (100 mg). And then stirred it at room temperature for 4 h. After the completion of the reaction, the resulting product was washed several times with deionized water and dried overnight, named NM125-D-A^0.

Text S3. Characterization of photocatalysts

The physical properties and chemical structure of the samples are determined using X-ray diffraction (XRD, XRD-6100, SHIMADZU, Japan), Inductive coupled plasma optical emission spectrometer (ICP-OES) (SPECTRO GENESIS, FES27, Germany), scanning electron microscopy (SEM, SU-1510, HITACHI, Japan), transmission electron microscope (TEM, JEM-F200, Japan), X-ray photoelectron spectroscopy (XPS, Thermo Scientific K-Alpha+, America), and N_2 adsorption-desorption isotherms (BET, ASAP-2020, USA). The optical properties are analyzed through UV-visible diffuse reflectance

spectroscopy (UV-vis DRS, UV-2700, SHIMADZU, Japan), Fourier transform infrared (FT-IR) spectra (Nicolet Apex, Thermo Scientific, USA), synchronous thermal analyzer (TGA) (STA499F3, NETZSCH, Germany), steady-state photoluminescence (PL, F-700, HITACHI, Japan, and FLS-1000, Edinburgh instruments), and photoelectrochemical analysis (FX-300, Perfectlight, China, and CHI660E, Chenhua, China). The mechanism of the photocatalytic reaction for the samples is investigated through free radical trapping experiments and the electron spin-resonance spectroscopy (ESR) (JES FA 200, Japan).

Text S4. Photocatalytic water decomposition to produce hydrogen

Typically, 18 mL acetonitrile, 2 mL triethanolamine, 0.2 mL deionized water, and 1 mL chloroplatinate acetonitrile solution (1 mg/mL) are added to the quartz reactor, respectively. Among them, acetonitrile is used as a solvent, triethanolamine is used as an electron sacrifice agent, deionized water is used as a proton source, and chloroplatinic acid is used as a cocatalyst. Then, 10 mg sample is added, the mixture is ultrasonically dispersed, and nitrogen is then injected into the mixture for 20 min to remove the air in the solution. Finally, a 300 W Xenon lamp is placed above the reactor and a 420 nm cut-off filter was installed to drive the photocatalytic hydrogen evolution reaction. In order to keep the reaction at a constant temperature, a constant temperature cooling circulation pump is equipped to keep the temperature of the reactor at 5 °C, and then the hydrogen generation is measured online by gas chromatography (GC 7920, Ceaulight, Beijing).

In addition, the apparent quantum yield (AQY) and energy conversion efficiency (STH) corresponding to hydrogen production are measured for the prepared samples under continuous illumination at 380, 420 and 500 nm.

$$AQY\ (\%)\ =\ \frac{N_e}{N_p}\ \times\ 100\% = \frac{2N_AR}{E\lambda/hc}$$

In this equation, N_e represents the total number of transferred electrons in the reaction and N_p represents the number of incident photons. R represents hydrogen production (mol), N_A represents Avogadro constant, E represents optical power (W), λ represents incident optical wavelength (nm), h represents Planck constant (J·s) and c represents the speed of light (m/s).

$$STH\ (\%)\ =\ \frac{\alpha\ \times\ \Delta G}{P_{light}\ \times\ S}\ \times\ 100\%$$

In this equation, α represents the hydrogen production efficiency (mmol/s), ΔG represents the Gibbs free energy (J/mol), P_{light} represents the energy flux of the incident light (mW/cm^2), and S represents the area of the reactor (cm^2).

Text S5. Photocatalytic NO purification

Initially, the sample (0.1 g) is sonicated in an ethanol solution to ensure homogenous dispersion. It is then evenly distributed in two Petri dishes with a diameter of 12 cm. After drying, the sample is placed in a rectangular glass reactor measuring 30 cm × 15 cm × 10 cm. Above the reactor, a Xenon lamp with a power of 300 W is placed and equipped with a 420 nm cut-off filter. The air flow (2.4 L/min) and NO gas flow (24 mL/min) are activated. Once the NO_x analyzer (Thermo Environmental

Instruments Inc., Model 42i-TL) detected a stable NO concentration of 550 ppb, the Xenon lamp is switched on for a duration of 30 min. After the designated time, the lamp is turned off.

$$\eta\,(\%) = (1 - \frac{C_t}{C_0}) \times 100\%$$

In this equation, C_t and C_0 represent the NO concentrations in the inlet and outlet air, respectively.

Text S6. *In-situ* DRIFTS spectra

For in-situ analysis of the intermediate species involved in the degradation of NO, the Rruker70v spectrometer (Harrick) equipped with an MCT detector is employed. The catalyst prepared is placed onto the surface of a diamond ATR crystal, followed by a 30 min vacuum treatment to eliminate adsorbed water molecules. Subsequently, a mixture of NO and O_2 is introduced into the gas pipeline, and after a 30 min adsorption of NO, the system is exposed to simulated visible light for 30 min to initiate photocatalytic oxidation. Infrared spectra are recorded every 2 min during the process, allowing for real-time monitoring of the changing molecular species.

Text S7. Electrochemical measurements

An electrochemical instrument with a three-electrode system was used to analyze electrochemical measurements. The working electrode was prepared as follows: add 50 μL H_2O, 450 μL ethanol, 10 μL Nafion, the sample (1 mg) and ultrasonic dispersion for 30 min, and then transferred 100 μL suspension to coat the ITO. The electrode was

dried in air at room temperature. The reference electrode was calomel electrode and the counter electrode was platinum electrode. Electrochemical impedance spectroscopy (EIS) and transient photocurrent tests were conducted in Na_2SO_4 (0.2 M). A xenon lamp (300 W) was treated as the light irradiation for photocurrent test.

Text S8. Theoretical calculations

The Vienna Ab Initio Package (VASP) is employed to perform all the density functional theory (DFT) calculations within the generalized gradient approximation (GGA) using the Perdew, Burke, and Enzerhof (PBE) formulation [1, 2]. The projected augmented wave (PAW) potentials are applied to describe the ionic cores and take valence electrons into account using a plane wave basis set with a kinetic energy cutoff of 450 eV [3, 4]. Partial occupancies of the Kohn–Sham orbitals are allowed using the Gaussian smearing method and a width of 0.05 eV. The 3×3×1 Monkhorst-Pack grid is used to sample the Brillouin region.

Supplementary Figures

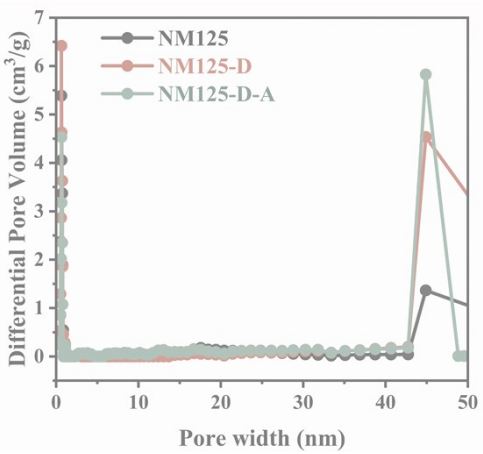

Fig. S1 Pore Parameters for NM125, NM125-D and NM125-D-A

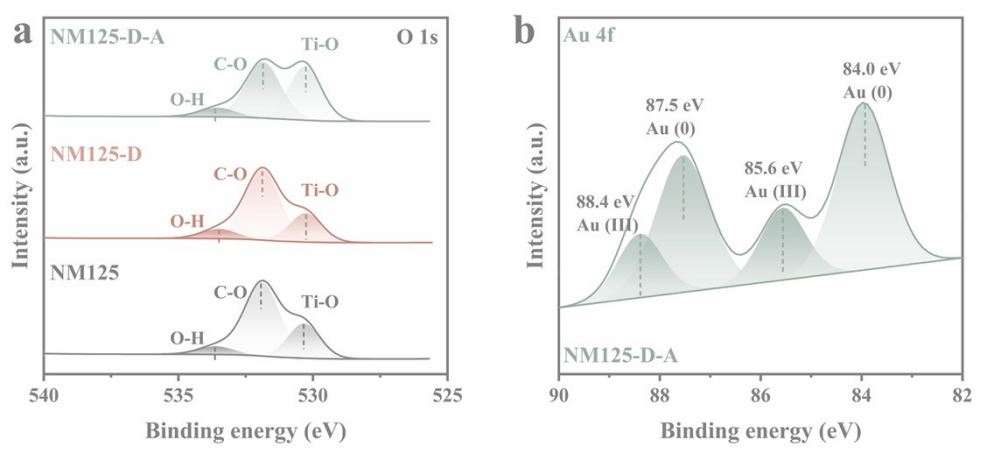

Fig. S2 (a) O 1s of NM125, NM125-D and NM125-D-A and (b) Au 4f of NM125-D-A

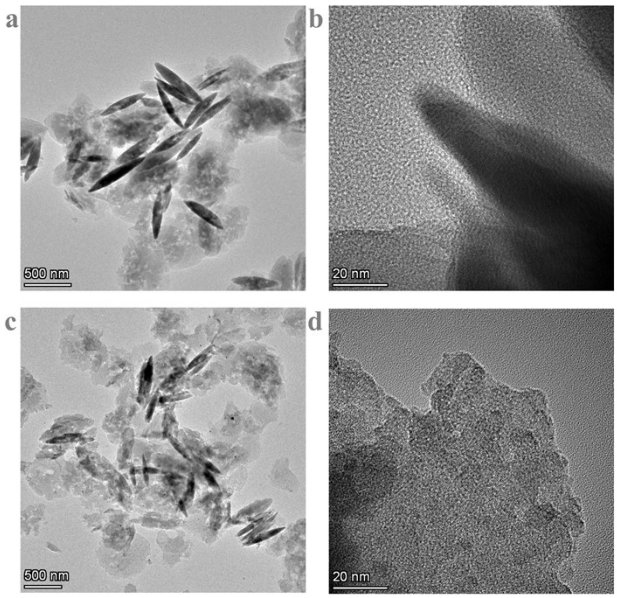

Fig. S3 TEM of (a-b) NM125-D and (c-d) NM125-D-A.

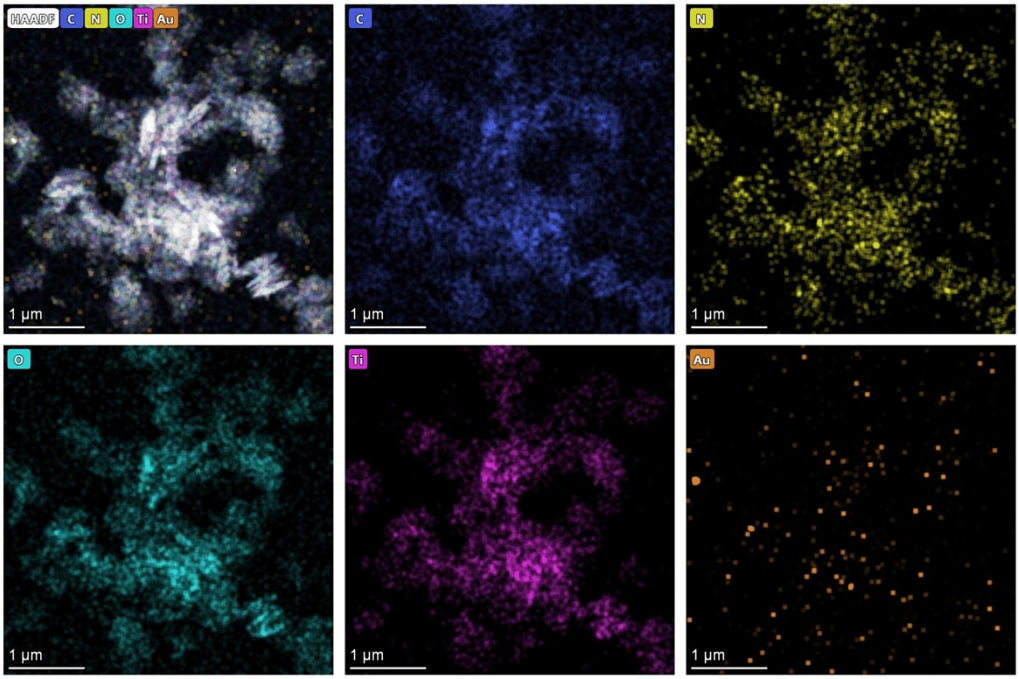

Fig. S4 TEM-EDS elemental mapping of NM125-D-A

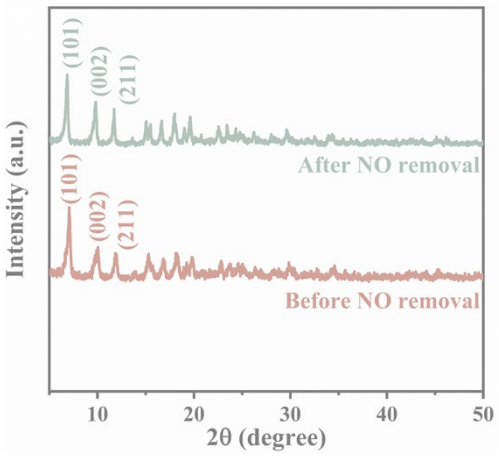

Fig. S5 XRD pattern of NM125-D-A before and after NO removal

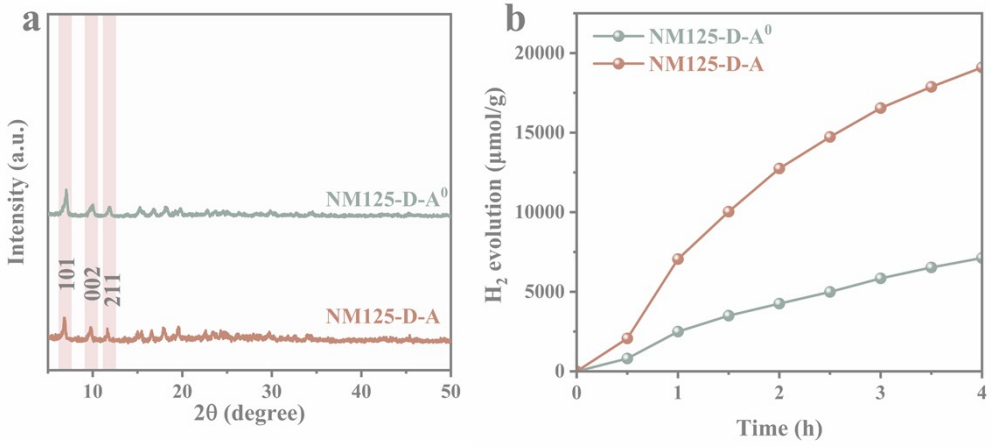

Fig. S6 (a) XRD pattern and (b) photocatalytic hydrogen evolution of NM125-D-A^0 and

NM125-D-A

We reduced the Au ions in NM125-D-A to the metallic state using glucose (denoted as NM125-D-A^0) [5]. XRD results (Fig. S6a) showed that the patterns of NM125-D-A^0 and NM125-D-A were highly consistent, indicating that the reduction process did not cause the collapse of the MOF framework. The results (Fig. S6b) showed that the hydrogen production rate of NM125-D-A^0 sharply decreased to 1780.90 μmol·g^{-1}·h^{-1}, which was much lower than that of NM125-D-A (4773.50 μmol·g^{-1}·h^{-1}).

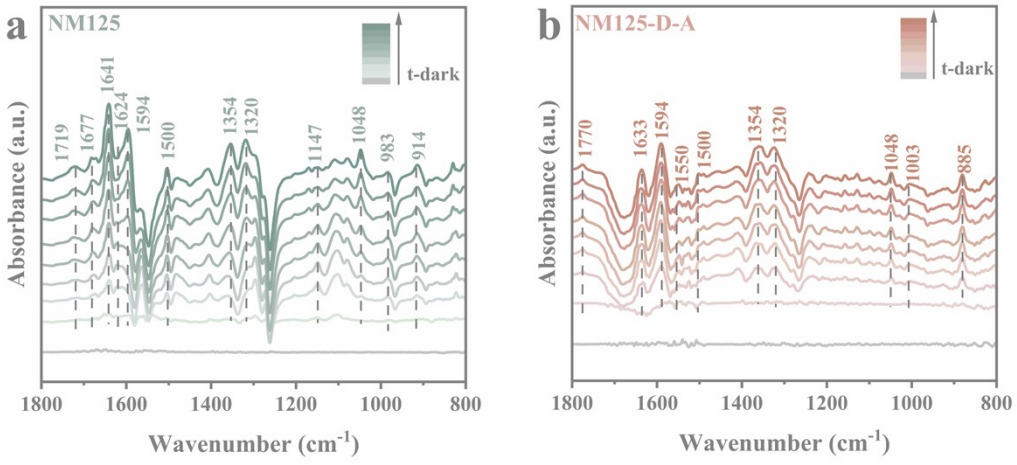

Fig. S7 *In-situ* infrared spectra of NO adsorption processes over (a) NM125 and (b) NM125-D-A

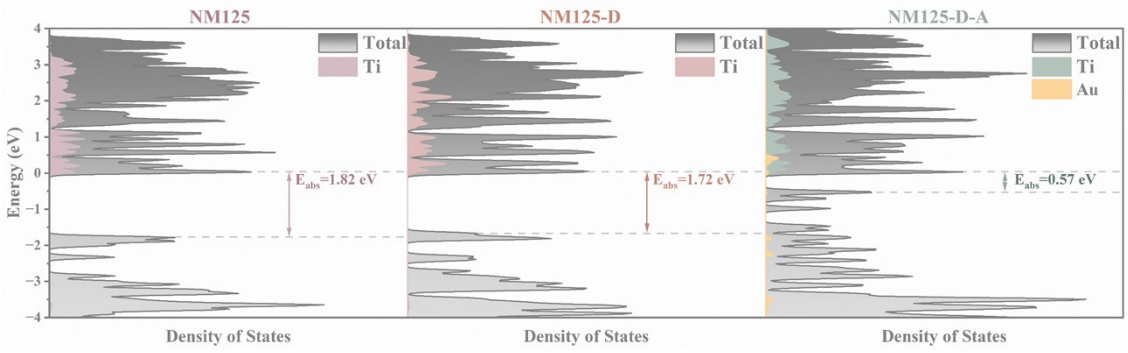

Fig. S8 Density of States (DOS) of NM125, NM125-D and NM125-D-A

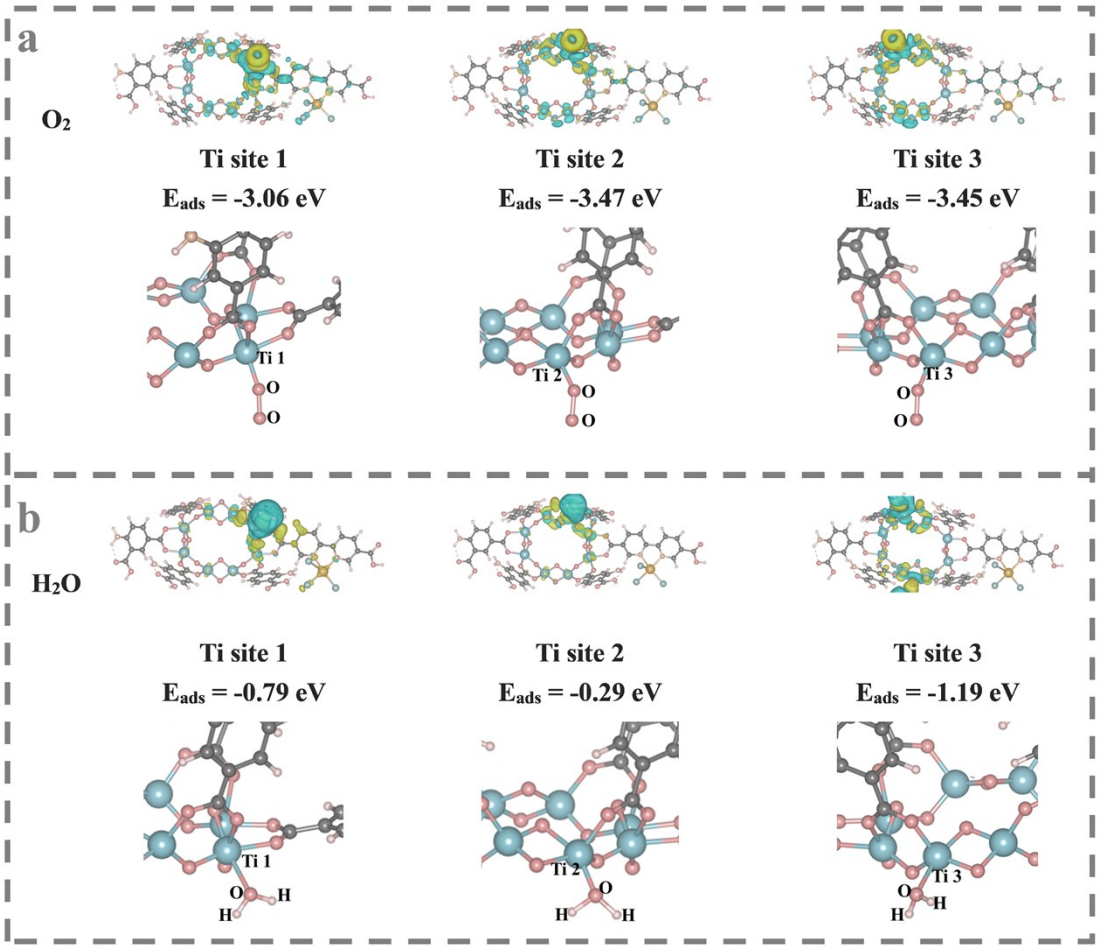

183

184 **Fig. S9** Adsorption of O_2 and H_2O molecule on different Ti sites in NM125-D-A.

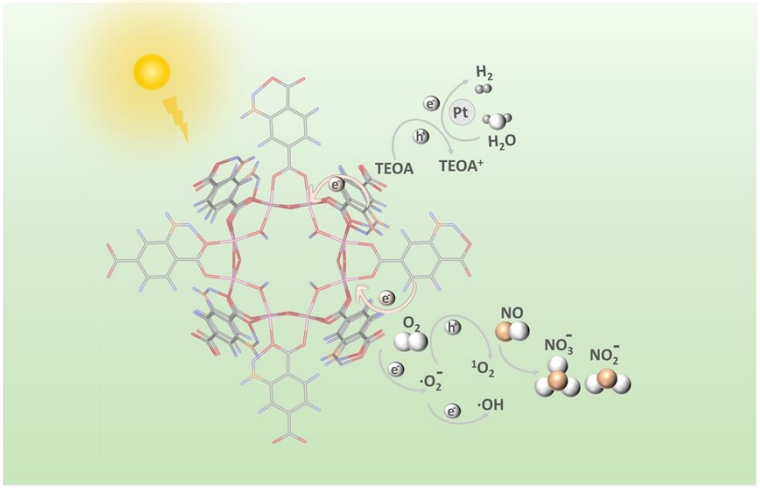

185

186 **Fig. S10** Possible photocatalytic mechanism of NM125

187 For the parent NM125 (Fig. S10), the ligand 2-Aminoterephthalic acid (NH_2-BDC)

188 acted as a light-harvesting antenna. Following photoexcitation, the generated charge

189 carriers were transferred to the Ti-oxo cluster, representing a conventional ligand-to-
190 metal charge transfer (LMCT) process. The Ti-oxo site then served as the active center
191 for the subsequent catalytic reactions.
192

Supplementary Tables

Table. S1. Au contents (wt %) of different samples characterized by ICP-OES

Sample	Au contents (wt %)
NM125-D-A	0.65

Table. S2. Specific Surface Area and Pore Parameters for NM125, NM125-D and NM125-D-A

Sample	BET surface area (m^2/g)	Total pore volume (cm^3/g)	Mesoporous pore volume (cm^3/g)	Average pore diameter (nm)
NM125	1165.43	0.627	0.178	2.15
NM125-D	1306.29	0.749	0.243	2.29
NM125-D-A	905.00	0.610	0.284	2.70

Table. S3. Comparison of photocatalytic hydrogen evolution data of MOF-based photocatalysts reported in recent years

Photocatalysts	Mass of photocatalyst	Light source	Sacrificial agents	Cocatalyst	H_2 Production rate	Ref.
NM125-D-A	10 mg	300 W Xe lamp, λ≥ 420 nm	TEOA	Pt	4773.50 $\mu mol \cdot g^{-1} \cdot h^{-1}$	This work
M-125-45-N	10 mg	300 W Xe lamp, λ≥ 420 nm	TEOA	Pt	3700 $\mu mol \cdot g^{-1} \cdot h^{-1}$	6
C/TiO_2/MIL-125	10 mg	132.6 mW LED lamp, λ≥ 400 nm	Methanol	—	314 $\mu mol \cdot g^{-1} \cdot h^{-1}$	7
W-MIL-125	25 mg	300 W Xe lamp, λ≥ 300	TEOA	Pt	1110.7 $\mu mol \cdot g^{-1} \cdot h^{-1}$	8

		nm				
MIL-125(Ti)/$ZnIn_2S_4$	100 mg	—	Na_2S/Na_2SO_3	—	873.4 μmol·g^{-1}·h^{-1}	9
g-C_3N_4/TiO_2/MIL-125	25 mg	300 W Xe lamp	Glycerol	NiS	1330 μmol·g^{-1}·h^{-1}	10
MIL-125-NH_2@TiO_2	5 mg	300 W Xe lamp, λ≥ 380 nm	TEOA	—	496 μmol·g^{-1}·h^{-1}	11
Pd/PdTCPP/NH_2-MIL-125	10 mg	300 W Xe lamp λ≥ 420 nm	TEOA	—	603 μmol·g^{-1}·h^{-1}	12
Co-CDs/NH_2-MIL-125	30 mg	300 W Xe lamp λ≥ 380 nm	TEOA	Pt	2261 μmol·g^{-1}·h^{-1}	13
Yb–NH_2-MIL-125	10 mg	300 W Xe lamp, λ≥ 420 nm	TEOA	Pt	1884 μmol·g^{-1}·h^{-1}	14
1 % PCN-222(Pd)/g-C_3N_4-AA	50 mg	300 W xenon lamp	TEOA	Pt	2338.17 μmol·g^{-1}·h^{-1}	15
Ti-MOF@P-Pt_1 SACs	10 mg	300 W xenon lamp, λ≥ 400 nm	TEOA	—	4193 μmol·g^{-1}·h^{-1}	16
TiO_2@NM/Ni10%	10 mg	300 W Xe lamp, λ≥ 420 nm	TEOA	—	1659.9 μmol·g^{-1}·h^{-1}	17
ENHM-2	10 mg	300 W Xe lamp	TEOA	Pt	2150 μmol·g^{-1}·h^{-1}	18
Ti_3C_2@MIL-NH_2	70 mg	300 W Xe arc lamp with an AM-1.5 filter	TEOA	—	4383.1 μmol·g^{-1}·h^{-1}	19
Au@NH_2-UiO-66/CdS	5 mg	300 W Xe lamp, λ≥ 420 nm	lactic acid	—	664.9 μmol·g^{-1}·h^{-1}	20

CdS/MIL-53(Fe)	5 mg	300 W Xe lamp, λ≥ 420 nm	benzyl alcohol	—	2334 μmol·g^{-1}·h^{-1}	21
CP@U6N	50 mg	300 W Xe lamp, λ≥ 400 nm	H_3PO_2	—	141.87 μmol·g^{-1}·h^{-1}	22
UNiMOF	50 mg	300 W Xe lamp, λ≥ 420 nm	TEOA	—	572 μmol·g^{-1}·h^{-1}	23
UiO-66@$ZnIn_2S_4$	40 mg	300 W Xe lamp, λ≥ 400 nm	TEOA	—	3061.61 μmol·g^{-1}·h^{-1}	24
Ni-BDC/Ni-TCPP-3	10 mg	300 W Xe lamp	TEOA	—	428.0 μmol·g^{-1}·h^{-1}	25
PdS@MIL-125-NH_2@ZnS	10 mg	225 W Xe lamp	TEOA	—	1164.2 μmol·g^{-1}·h^{-1}	26
CdS/Ni-MOF	30 mg	300 W Xe lamp, λ≥ 420 nm	lactic acid	—	2508 μmol·g^{-1}·h^{-1}	27
MOF-5/CuO@$ZnIn_2S_4$	100 mg	300 W Xe lamp	Methanol	—	1938.3 μmol·g^{-1}·h^{-1}	28
NH_2-MIL-125/Co(dmgH)$_2$	10 mg	300 W Xe lamp, λ≥ 420 nm	TEOA	—	2195 μmol·g^{-1}·h^{-1}	29

Table. S4. Comparison of photocatalytic NO removal data of MOF-based photocatalysts reported in recent years

Photocatalysts	Mass of photocatalyst	Light source	NO removal rate	Ref.
NM125-D-A	100 mg	300 W Xe lamp, λ≥ 420 nm	65.04%	This work
N/C/MIL-125(Ti)	100 mg	300 W Xe lamp, λ≥ 420 nm	49%	30
Co-CDs-NH_2-MIL-125	100 mg	12 W LED lamp	67.6%	31

Au/MIL-125-NH_2(Ti)/PdTCPP	100 mg	150 W tungsten halogen lamp	63.72%	[32]
TiO_2/NH_2–MIL-125(Ti)	200 mg	150 W tungsten halogen lamp, λ≥ 420 nm	68.08%	[33]
Defect-NH_2-MIL-125/Eosin Y	200 mg	150 W tungsten halogen lamp, λ≥ 420 nm	62.05%	[34]
Au@NH_2-MIL-125(Cu/Ti)	100 mg	12 W LED lamp	43%	[5]
STO/GQDs/NU6	100 mg	300 W Xe lamp, λ≥ 400 nm	69.0%	[35]
CN/NU6	100 mg	300 W Xe lamp, λ≥ 400 nm	65.4%	[36]
GO/NH_2-MIL-125(Ti)	50 mg	two 150 W tungsten halogen lamp, λ≥ 420 nm	50%	[37]
65-NH_2-MIL-125	100 mg	12 W LED lamp	65.49%	[38]
Protonated NH_2-MIL-125	100 mg	12 W LED lamp	49.17%	[39]

Table. S5. Band structure of NM125, NM125-D and NM125-D-A

Material	Band gap (E_g, eV)	Conduction band (E_{CB}, V)	Valence band (E_{VB}, V)
NM125	2.66	-0.61	2.05
NM125-D	2.62	-0.76	1.86
NM125-D-A	2.57	-0.83	1.74

Table. S6. Substances corresponding to infrared peak values during dark adsorption and photocatalytic oxidation stages

	NM125			NM125-D-A		
	Wavenumber (cm^{-1})	Band attribution	Ref.	Wavenumber (cm^{-1})	Band attribution	Ref.
Adsorption process	914, 1677	N_2O_4	[40, 41]	885, 1320	NO_2	[42, 43]

	983, 1354, 1594, 1719	NO_2^-	[44-46]	1003, 1048, 1500, 1550, 1770	NO_3^-	[30, 46-48]
	1048, 1500	NO_3^-	[48]			
	1147, 1641	NO	[49, 50]	1354, 1594, 1633	NO_2^-	[45, 46]
	1320, 1624	NO_2	[43]			
Photocatalytic process	914, 1677	N_2O_4	[40, 41]	885, 1320	NO_2	[42, 43]
	983, 1354, 1594, 1719	NO_2^-	[44-46]	1003, 1048, 1102, 1500, 1550, 1770	NO_3^-	[30, 39, 46-48]
	871, 1048, 1122, 1500	NO_3^-	[48, 51, 52]			
	1147, 1641	NO	[49, 50]	1354, 1594, 1633	NO_2^-	[45, 46]
	1320	NO_2	[43]	1725	N_2O_4	[53]

Table. S7. The reaction pathway for NO removal

Generation of reactive species of NM125-D-A

$$NM125\text{-}D\text{-}A + h\nu \rightarrow e^- + h^+ \quad (1)$$

$$e^- + O_2 \rightarrow \bullet O_2^- \quad (2)$$

$$h^+ + \bullet O_2^- \rightarrow {}^1O_2 \quad (3)$$

$$e^- + \bullet O_2^- + 2H^+ \rightarrow H_2O_2 \quad (4)$$

$$H_2O_2 + e^- \rightarrow \bullet OH + OH^- \quad (5)$$

Photocatalytic removal of NO reaction of NM125-D-A

$$2NO + O_2 \rightarrow 2NO_2 \quad (6)$$

$$2NO_2 \rightleftharpoons N_2O_4 \quad (7)$$

$$2NO + 2e^- + O_2 \rightarrow 2NO_2^- \quad (8)$$

$$NO + e^- + 2\bullet OH \rightarrow NO_2^- + H_2O \quad (9)$$

$$NO + \bullet O_2^- \rightarrow NO_3^- \quad (10)$$

$$2NO_2 + \bullet O_2^- \rightarrow 2NO_3^- \quad (11)$$

$$NO_2 + \bullet OH \rightarrow NO_3^- + H^+ \quad (12)$$

$$2NO_2^- + \bullet O_2^- + h^+ \rightarrow 2NO_3^- \quad (13)$$

$$2NO_2^- + {}^1O_2 \rightarrow 2NO_3^- \quad (14)$$

Table. S8. The reaction pathway for H_2 production

$$NM125\text{-}D\text{-}A + h\nu \leftrightarrow e^- + h^+ \quad (1)$$

$$TEOA + h^+ \rightarrow TEOA^+ \quad (2)$$

$$H_2O \leftrightarrow OH^- + H^+ \quad (3)$$

$$2H^+ + 2e^- \rightarrow H_2 \quad (4)$$

References

1. G. Kresse and D. Joubert, *Phys. Rev. B*, 1999, **59**, 1758.
2. J. P. Perdew, K. Burke and M. Ernzerhof, *Phys. Rev. Lett.*, 1996, **77**, 3865-3868.
3. G. Kresse and J. Furthmüller, *Phys. Rev. B Condens. Matter*, 1996, **54**, 11169-11186.
4. S. Grimme, J. Antony, S. Ehrlich and H. Krieg, *J. Chem. Phys.*, 2010, **132**, 154104.
5. Y. He, H. Li, J. Wu, Z. Liu, Y. Chen, W. Guo, Y. Wu, M. Fu and X. Liu, *Appl. Surf. Sci.*, 2022, **604**, 154641.
6. X. Liu, K. Wu, C. Jia, Y. He, Y. Qiu, Y. Fang, H. Ma, S. Wang, S. Wei and F. Dong, *J. Colloid Interface Sci.*, 2025, **680**, 948-964.
7. Y. Zhao, N. Yang, T. Zhou, W. Zhan, J. Zhao, M. Chen, T. He, J. Zhang, Y. Zhang, G. Zhang and Q. Liu, *Int. J. Hydrogen Energy*, 2024, **65**, 151-157.
8. Y. Zhang, F. Mao, Y. Liu, X. Wu, C. Wen, S. Dai, P. Liu and H. Yang, *Sci. China Mater.*, 2022, **65**, 1237-1244.
9. T. Liu, B. Wang, M. Wang, J. Gu, W. Wang, H. Shen and J. Zhang, *J. Mater. Sci.*, 2024, **59**, 1253-1264.
10. B. Tatykayev, B. Chouchene, L. Balan, T. Gries, G. Medjahdi, E. Girot, B. Uralbekov and R. Schneider, *Nanomaterials*, 2020, **10**, 1387.
11. B. Zhang, J. Zhang, X. Tan, D. Shao, J. Shi, L. Zheng, J. Zhang, G. Yang and B. Han, *ACS Appl. Mater. Interfaces*, 2018, **10**, 16418-16423.
12. C. Jia, Y. Wang, R. Zeng, X. Liu, Y. You, Y. Feng, S. Wang, Y. He, S. Li and S. Wei, *Mol. Catal.*, 2024, **556**, 113925.
13. Y. He, S. Luo, Y. Tan, M. Chen, H. Zhou, J. Yu, L. Pu, Y. Huang, M. Fu and X. Liu, *J. Alloys Compd.*, 2022, **913**, 165226.
14. H. Li, X. Liu, H. Feng, J. Zhao, P. Lu, M. Fu, W. Guo, Y. Zhao and Y. He, *Catal. Sci. Technol.*, 2021, **11**, 6225-6233.
15. Y. Li, W. Qin, X. Li, Q. Zhu, F.-q. Bai and T. Tian, *Chem. Eng. J.*, 2025, 168119.
16. Y. Zhu, N. Song, S. Liu, K. Zhang, B. Liu and Y. Wang, *Green Chem.*, 2025, **27**,

7973-7981.
17. J. Li, H. Chang, S. Feng, H. Jian, Q. Shen, X. Liu, H. Jia and J. Xue, *Chem. Eng. J.*, 2024, **498**, 155542.
18. Y. Liu, X. Xin, Y. Shi, Z. Zhao, J. Tan, D. Yang and Z. Jiang, *Chem. Eng. J.*, 2024, **482**, 149193.
19. Y. Li, Y. Liu, Z. Wang, P. Wang, Z. Zheng, H. Cheng, Y. Dai and B. Huang, *Chem. Eng. J.*, 2021, **411**, 128446.
20. Z. Li, J. Zi, X. Luan, Y. Zhong, M. Qu, Y. Wang and Z. Lian, *Adv. Funct. Mater.*, 2023, **33**, 2303069.
21. P. Li, X. Yan, S. Gao and R. Cao, *Chem. Eng. J.*, 2021, **421**, 129870.
22. Y.-Y. Wang, X.-Y. Ji, M. Yu and J. Tao, *Mater. Chem. Front.*, 2021, **5**, 7796-7807.
23. A. Cao, M. Zhang, X. Su, V. Romanovski and S. Chu, *ACS Appl. Nano Mater.*, 2022, **5**, 5416-5424.
24. X. Peng, L. Ye, Y. Ding, L. Yi, C. Zhang and Z. Wen, *Appl. Catal. B: Environ.*, 2020, **260**, 118152.
25. Y. Ma, H.-X. Fang, R. Chen, Q. Chen, S.-J. Liu, K. Zhang and H.-J. Li, *Rare Met.*, 2023, **42**, 3993-4004.
26. Z. Tai, G. Sun, T. Wang, Z. Li and J. Tai, *J. Mater. Sci. Technol.*, 2023, **145**, 116-124.
27. J. Guo, Y. Liang, L. Liu, J. Hu, H. Wang, W. An and W. Cui, *Appl. Surf. Sci.*, 2020, **522**, 146356.
28. Y. Yang, Z. Xing, W. Kong, C. Wu, H. Peng, Z. Li and W. Zhou, *Nanoscale*, 2022, **14**, 14741-14749.
29. S. Luo, X. Liu, X. Wei, M. Fu, P. Lu, X. Li, Y. Jia, Q. Ren and Y. He, *J. Hazard. Mater.*, 2020, **399**, 122824.
30. M. Chen, X. Wei, L. Zhao, Y. Huang, S.-c. Lee, W. Ho and K. Chen, *Ind. Eng. Chem. Res*, 2020, **59**, 6470-6478.
31. S. Luo, Y. Zheng, W. Xia, M. Mao, Y. He, X. Liu and J. Wang, *Sep. Purif. Technol.*, 2025, **355**, 129737.
32. Y. Li, J. Zhou, X. He, Y. He, J. Jing, X. Liu, S. Li and S. Wei, *J. Alloys Compd.*, 2024, **1002**, 175428.
33. M. Xu, P. Zhu, Q. Cai, M. Bu, C. Zhang, H. Wu, Y. He, M. Fu, S. Li and X. Liu, *Chin. Chem. Lett.*, 2024, **35**, 109524.
34. M. Xu, Y. Xu, C. Zhang, S. Chen, X. Liu, H. Wu, S. Li, Y. He and F. Dong, *Sep. Purif. Technol.*, 2023, **322**, 124374.
35. Z. Zhou, D. Chen, S. Dong, N. Li, Q. Xu, H. Li, J. He and J. Lu, *Ind. Eng. Chem. Res.*, 2022, **61**, 3550-3560.
36. Z. Zhou, D. Chen, N. Li, Q. Xu, H. Li, J. He and J. Lu, *Chem. Eng. J.*, 2021, **418**, 129117.
37. X. Li, Z. Le, X. Chen, Z. Li, W. Wang, X. Liu, A. Wu, P. Xu and D. Zhang, *Appl. Catal. B: Environ.*, 2018, **236**, 501-508.
38. Y. He, Y. Tan, M. Song, Q. Tu, M. Fu, L. Long, J. Wu, M. Xu and X. Liu, *J. Hazard. Mater.*, 2022, **430**, 128468.
39. S. Luo, C. Zhang, X. Liu, Y. Li, L. Tang, M. Fu, S. Wang, J. Wu, M. Xu, X. Wang and

Y. He, *Chem. Eng. J.*, 2022, **432**, 134244.
40. C. Wang, M. Fu, J. Cao, X. Wu, X. Hu and F. Dong, *Chem. Eng. J.*, 2020, **385**, 123833.
41. W. Huo, W. Xu, T. Cao, Z. Guo, X. Liu, G. Ge, N. Li, T. Lan, H.-C. Yao, Y. Zhang and F. Dong, *J. Colloid Interface Sci.*, 2019, **557**, 816-824.
42. F. Zhong, C. Yuan, Y. He, Y. Sun, J. Sheng and F. Dong, *J. Hazard. Mater.*, 2022, **438**, 129463.
43. W. Yang, Q. Ren, F. Zhong, Y. Wang, J. Wang, R. Chen, J. Li and F. Dong, *Nanoscale*, 2021, **13**, 20601-20608.
44. Y. Liu, S. Yu, Z. Zhao, F. Dong, X. A. Dong and Y. Zhou, *J. Phys. Chem. C*, 2017, **121**, 12168-12177.
45. R. Chen, H. Wang, H. Wu, J. Sheng, J. Li, W. Cui and F. Dong, *Chin. J. Catal.*, 2020, **41**, 710-718.
46. X. Li, Q. Dong, F. Li, Q. Zhu, Q. Tian, L. Tian, Y. Zhu, B. Pan, M. Padervand and C. Wang, *Appl. Catal. B Environ.*, 2024, **340**, 123238.
47. R. Li, X. Liu, Y. Tang, J. Yu, Y. Chen, M. Fu, S. Li and Y. He, *Sep. Purif. Technol.*, 2023, **306**, 122598.
48. J. Li, X. a. Dong, Y. Sun, G. Jiang, Y. Chu, S. C. Lee and F. Dong, *App. Catal. B: Environ.*, 2018, **239**, 187-195.
49. K. Li, H. Wang, L. Chen, J. Li and F. Dong, *App. Catal. B: Environ.*, 2022, **312**, 121423.
50. R. Li, Z. Wu, Y. Chen, X. Liu, W. Guo, Y. Huang, M. Fu and Y. He, *Fuel*, 2023, **336**, 126766.
51. K. Li, W. Cui, J. Li, Y. Sun, Y. Chu, G. Jiang, Y. Zhou, Y. Zhang and F. Dong, *Chem. Eng. J.*, 2019, **378**, 122184.
52. G. Jiang, X. Li, M. Lan, T. Shen, X. Lv, F. Dong and S. Zhang, *App. Catal. B: Environ.*, 2017, **205**, 532-540.
53. M. Sun, W. Zhang, Y. Sun, Y. Zhang and F. Dong, *Chin. J. Catal.*, 2019, **40**, 826-836.